Chemical Science

ROYAL SOCIETY OF CHEMISTRY

EDGE ARTICLE

View Article Online
View Journal | View Issue

Cite this: *Chem. Sci.*, 2023, **14**, 10264

All publication charges for this article have been paid for by the Royal Society of Chemistry

Received 2nd June 2023
Accepted 2nd September 2023

DOI: 10.1039/d3sc02836d

rsc.li/chemical-science

Lewis acid-driven self-assembly of diiridium macrocyclic catalysts imparts substrate selectivity and glutathione tolerance†

Hieu D. Nguyen, Rahul D. Jana, Dylan T. Campbell, Thi V. Tran and Loi H. Do *

Molecular inorganic catalysts (MICs) tend to have solvent-exposed metal centers that lack substrate specificity and are easily inhibited by biological nucleophiles. Unfortunately, these limitations exclude many MICs from being considered for *in vivo* applications. To overcome this challenge, a strategy to spatially confine MICs using Lewis acid-driven self-assembly is presented. It was shown that in the presence of external cations (*e.g.*, Li^+, Na^+, K^+, or Cs^+) or phosphate buffered saline, diiridium macrocycles spontaneously formed supramolecular iridium-cation species, which were characterized by X-ray crystallography and dynamic light scattering. These nanoassemblies selectively reduced sterically unhindered C=O groups *via* transfer hydrogenation and tolerated up to 1 mM of glutathione. In contrast, when non-coordinating tetraalkylammonium cations were used, the diiridium catalysts were unable to form higher-ordered structures and discriminate between different aldehyde substrates. This work suggests that *in situ* coordination self-assembly could be a versatile approach to enable or enhance the integration of MICs with biological hosts.

Introduction

Bioorthogonal chemistry has allowed researchers to study and manipulate living systems with high precision and efficiency.[1–4] It has extensive biomedical applications, from the labelling of disease targets to the *in vivo* generation of therapeutic drugs. Metal-free click reactions such as strain-promoted azide–alkyne cycloaddition[5] and inverse electron-demand Diels–Alder[6] are among the most widely used methods. There is growing interest in expanding the bioorthogonal chemistry library by leveraging metal catalysis.[7–11] For example, molecular inorganic catalysts (MICs) have been used to mediate intracellular C–C bond cross-coupling,[12] olefin metathesis,[13,14] protecting group cleavage,[15–18] transfer hydrogenation,[19,20] and others.[21–23] Unfortunately, since MICs lack the ability to restrict access to their active sites, they are prone to inhibition by endogenous thiols[21,24,25] and have poor substrate selectivity. These deficiencies severely limit their practical applications in living environments.

To enhance their biocompatibility, MICs can be spatially confined[26–30] within macromolecular hosts[31–33] or designer ligands[34–36] (Chart 1A). For example, Ward and coworkers reported that organoiridium complexes incorporated into human carbonic anhydrase II were capable of catalyzing transfer hydrogenation reactions in the periplasm of *E. coli* bacteria.[37] These artificial metalloenzymes achieved turnover numbers of >90. In another example, Zimmerman and coworkers constructed metal–organic nanoparticles by crosslinking single polymer chains containing copper ions.[38,39] These complexes

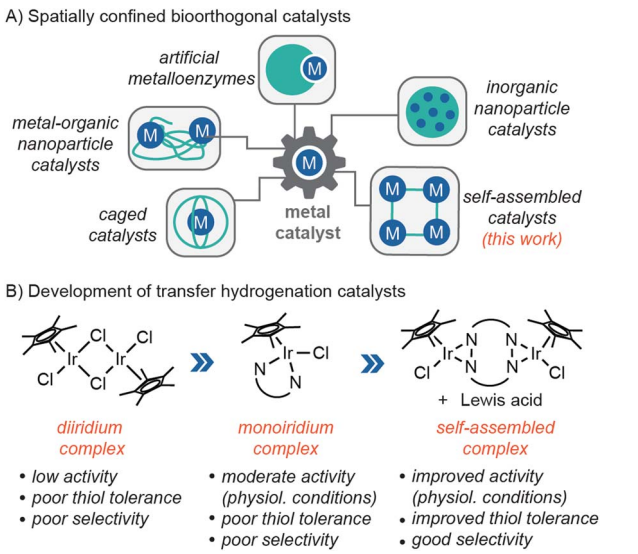

Chart 1 Examples of spatially confined bioorthogonal catalysts (A) and chemical optimization of transfer hydrogenation catalysts (B).

Department of Chemistry, University of Houston, 4800 Calhoun Road, Houston, Texas, USA. E-mail: loido@uh.edu

† Electronic supplementary information (ESI) available. CCDC 2267222. For ESI and crystallographic data in CIF or other electronic format see DOI: https://doi.org/10.1039/d3sc02836d

have low toxicity and were used to synthesize anti-microbial agents inside *E. coli*. In recent work, Martinez, Colomban and coworkers developed caged catalysts comprising Cu(I) centers supported by hemicryptophane ligands. These caged MICs catalyzed azide–alkyne cycloaddition in the presence of excess glutathione (GSH).[40] A caveat, however, is that these reactions were not performed under biologically relevant conditions (*e.g.*, they were conducted in $MeOH/CH_2Cl_2$ solutions). Other researchers have reported the use of inorganic nanoparticle catalysts for in-cell catalysis, but these materials are not based on MICs.[41–44] Although the confinement strategies above have been demonstrated to be effective in some cases, they also have limitations. For example, macromolecular catalysts may not be able to cross the blood–brain barrier due to their large size[45] and some MICs may not be easily converted into caged species.

In our bioorthogonal catalyst discovery program, we use an iterative approach to engineer MICs with improved biocompatibility. In previous work, we found that $[Cp^*IrCl_2]_2$ (Cp^* = pentamethylcyclopentadienyl anion) was a poor transfer hydrogenation catalyst under physiologically relevant conditions (Chart 1B).[46] This complex is too kinetically labile to form single component species necessary for efficient catalysis. When the Cp*Ir unit was ligated with *N*-phenylpicolinamidate to give [Cp*Ir(*N*-phenylpicolinamidate)Cl] (**Ir1**), high catalytic activity was observed in aqueous solutions.[46,47] Surprisingly, other bidentate donors such as 2,2′-bipyridine or 2-phenylpyridine did not produce viable Ir catalysts. Despite its high intrinsic activity, **Ir1** is prone to catalyst inhibition by thiols due to its unprotected half-sandwich structure. Although **Ir1** was used successfully to perform transfer hydrogenation in living cells,[19] its catalytic efficiency is likely low due to their potential to be deactivated in the biological milieu.

In the present work, to protect **Ir1**, we created a macrocyclic platform that would accommodate two Cp*Ir units to give **Ir2** (Scheme 1). In addition to being easier to synthesize than a caged catalyst, **Ir2** also contains backbone amides that are capable of binding external Lewis acids, reminiscent of amino acid side chains inside biological ion channels.[48,49] We discovered that combining **Ir2** with alkali ions led to the formation of higher-ordered structures, which exhibited improved tolerance towards glutathione and reacted preferentially with small aldehyde substrates under physiologically relevant conditions. Although supramolecular metal–organic complexes have been used in biological applications,[50–52] bioorthogonal catalysts formed *in situ via* metal–ligand coordination are unprecedented to the best of our knowledge. Our work suggests that coordination self-assembly may complement other MIC confinement strategies[26] and provide a convenient way to endow catalysts with emergent properties.[53,54] In particular, the ability to discriminate between sterically hindered *vs.* unhindered carbonyl groups could be useful in biological aldehyde detoxification.[55–57]

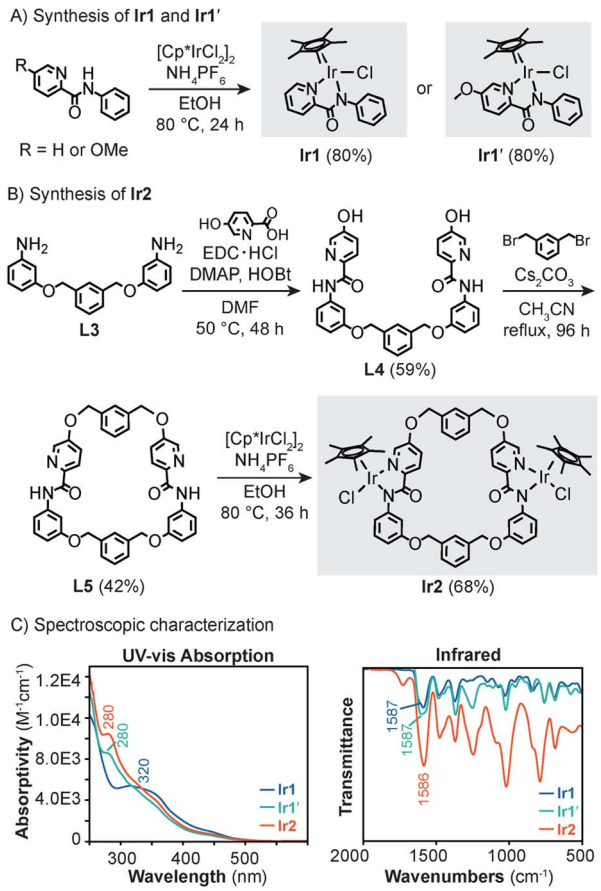

Scheme 1 Synthesis of monoiridium **Ir1** and **Ir1′** (A) and diiridium **Ir2** (B) and their UV-vis absorption (CH_2Cl_2, RT) and infrared spectra (C).

Results and discussion

Because **Ir1** lacks steric shielding on one hemisphere due to its half-sandwich structure, it can interact with external species of varying shapes and sizes. This feature is problematic because the catalyst can be readily poisoned by endogenous components and is unable to differentiate between functionally similar substrates. We reasoned that if two **Ir1** units could be linked through several attachment points, the iridium centers would be spatially confined by restricting their rotational freedom. Based on this rationale, we synthesized the symmetric **Ir2** complex, which has the formula $[Cp^*_2Ir_2(\text{ligand } \mathbf{L5})Cl_2]$ (Scheme 1B). The ligand **L5** was prepared starting from precursor **L3**, which contains 3-aminophenol units flanking a *m*-xylene spacer. Combining **L3** with 5-hydroxypicolinic acid in the presence of *N*-(3-dimethylaminopropyl)-*N*′-ethylcarbodiimide hydrochloride (EDC·HCl), 4-(dimethylamino) pyridine (DMAP), and *N*-hydroxybenzotriazole (HOBt) provided **L4** in 59% yield. Template-assisted ring closing by treating **L4** with aliquots of *m*-xylylene dibromide and Cs_2CO_3 over a period of 96 h under dilute conditions afforded **L5** as a white solid (42% yield). Finally, **Ir2** was obtained by stirring **L5** with $[Cp^*IrCl_2]_2$ and NH_4PF_6 at 80 °C for 36 h to furnish a yellow solid in 68% yield after purification by silica gel column chromatography. As catalyst standards, we also prepared **Ir1** (ref. 58) and a variant bearing *N*-phenyl-5-methoxypicolinamidate (**Ir1′**) (Scheme 1A). The latter was designed to be a mononuclear

analogue of **Ir2**, except that it lacks the ability to coordinate with Lewis acids as will be demonstrated in a later section.

Spectroscopic characterization of the mono- and diiridium complexes revealed that they exhibit similar features (Scheme 1C). For example, the ultraviolet-visible (UV-vis) absorption spectra of **Ir1**′ and **Ir2** were nearly identical, showing a prominent band centered at 280 nm. In contrast, **Ir1** has an absorption maximum at 320 nm. All three complexes displayed C=O vibrational stretches at ~1590 cm^{-1}, suggesting that the amidate groups donate electron density to their respective metal centers to the same extent. These results indicate that the Ir centers in **Ir1**, **Ir1**′, and **Ir2** are electronically similar despite the latter having a more sterically crowded environment due to the macrocycle structure. Thus, the effects of spatial confinement on the catalyst behavior could be teased out by comparing the reactivity of **Ir1**/**Ir1**′ *vs.* **Ir2**.

To test its transfer hydrogenation activity under biologically relevant conditions, **Ir2** (0.5 mol% relative to substrate) was combined with benzaldehyde and excess sodium formate (HCOONa) in various mixtures at 37 °C for 24 h. About 10% v/v of DMSO was needed to sufficiently solubilize **Ir2**. Our results showed that >80% yield of benzyl alcohol was obtained in H_2O/DMSO and phosphate buffered saline (PBS)/DMSO (Fig. 1A). The use of cell culture media such as Roswell Park Memorial Institute (RPMI) 1640 and Dulbecco's Modified Eagle Medium (DMEM), with or without fetal bovine serum (FBS), lowered the reaction yield to below 50%. The presence of glutamine (Gln), lysine (Lys), or arginine (Arg) as additives had minimal effects on **Ir2** (~70–80% yield). However, having high concentrations (5–25 mM) of glucose (Glc) reduced the reaction efficiency to ≤52% yield. In previous studies,[46] we also observed that **Ir1** was more active in PBS than in cell culture media, which was attributed to the inhibiting effects of sulfur- and nitrogen-containing species present in the latter.

To assess the potential of **Ir2** to be applied in living systems, we measured its effects on NIH-3T3 mouse fibroblast cells after treatment for 24 h (Fig. 1B). Our results showed that the half-maximal inhibition concentration (IC_{50}) of **Ir2** was 85 μM, which is higher than that for **Ir1** (IC_{50} = 62 μM), suggesting that the former may be less cytotoxic than the latter. To determine whether the iridium complexes are cell permeable, we measured the iridium content of NIH-3T3 cells treated with either **Ir1** or **Ir2** for 24 h (Table S13 and Fig. S74†). Our inductively coupled plasma mass spectrometric (ICP-MS) results showed that the cells contained about 1.7× more **Ir2** than **Ir1** (1487 *vs.* 858 ng Ir/10^6 cells, respectively).[57] Based on these cytotoxicity and cellular uptake data, **Ir2** will likely be compatible with biological hosts at low catalyst loadings (*i.e.*, below its IC_{50}).

We evaluated the substrate scope of **Ir2** under our standard transfer hydrogenation conditions (Fig. 2). In these experiments, an aldehyde was combined with **Ir2** (0.5 mol% relative to

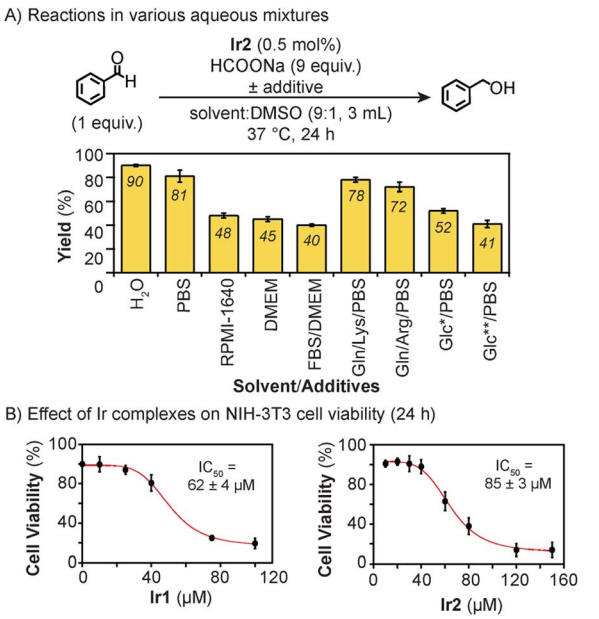

Fig. 1 (A) Comparison of the transfer hydrogenation yield using **Ir2** in various aqueous media. Abbreviations: PBS = phosphate buffered saline, RMPI = Roswell Park Memorial Institute, DMEM = Dulbecco's Modified Eagle Medium, FBS = fetal bovine serum, Gln = glutamine, Lys = lysine, Arg = arginine, Glc = glucose. Single asterisk (*) = 5 mM; double asterisk (**) = 25 mM. (B) Cell viability curves for **Ir1** and **Ir2** in NIH-3T3 cells after 24 h exposure.

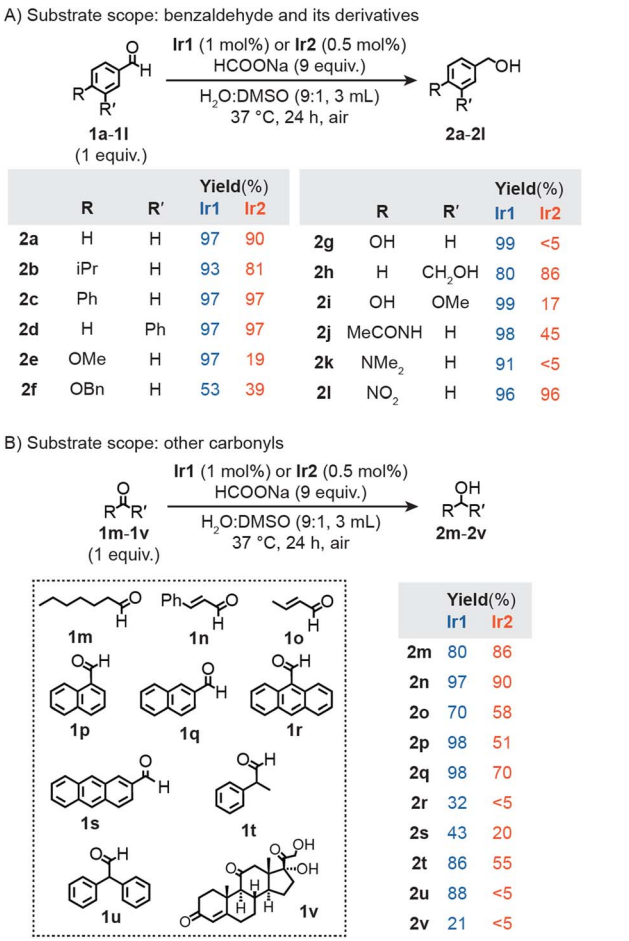

	R	R′	Yield(%) Ir1	Ir2
2a	H	H	97	90
2b	iPr	H	93	81
2c	Ph	H	97	97
2d	H	Ph	97	97
2e	OMe	H	97	19
2f	OBn	H	53	39
2g	OH	H	99	<5
2h	H	CH_2OH	80	86
2i	OH	OMe	99	17
2j	MeCONH	H	98	45
2k	NMe_2	H	91	<5
2l	NO_2	H	96	96

	Yield(%) Ir1	Ir2
2m	80	86
2n	97	90
2o	70	58
2p	98	51
2q	98	70
2r	32	<5
2s	43	20
2t	86	55
2u	88	<5
2v	21	<5

Fig. 2 Transfer hydrogenation studies using **Ir1** or **Ir2** and HCOONa with benzaldehyde and its derivatives (A) or other carbonyl-containing (B) substrates.

substrate) and HCOONa as the hydride source in H_2O/DMSO (9 : 1) at 37 °C under air for 24 h. Reactions of benzaldehyde or its derivatives featuring non-polar substituents (**1a–1d**) gave the corresponding benzyl alcohol (**2a–2d**) in excellent yields (>80%) (Fig. 2A). Benzaldehyde variants with electron-withdrawing 3-carbonyl (**1h**) or 4-nitro (**1l**) groups were also reduced efficiently (86 and 96% yield of **2h** and **2l**, respectively). In contrast, benzaldehyde substrates with electron-donating groups (*e.g.*, 4-methoxy in **1e**, 4-benzyloxy in **1f**, 4-hydroxy in **1g**, 4-hydroxy-3-methoxy in **1i**, 4-acetylamino in **1j**, and 4-dimethylamino in **1k**) afforded yields of the alcohol products below 50%.

A similar set of reactions were performed using the mono-iridium complexes, except that the catalyst loading was doubled to 1.0 mol% (relative to substrate) so that the same amount of iridium was used as in the **Ir2** reactions. Our data showed that in the presence of HCOONa, **Ir1** converted nearly all benzaldehydes to their corresponding benzyl alcohols with almost quantitative yields (Fig. 2A). The lower yield of **2f** (53%) from **1f** is presumably due to the steric hindrance of the benzyloxy (OBn) group. Since this substituent was not cleaved under our transfer hydrogenation conditions, it suggests that the OBn moiety in the **Ir2** macrocycle is unaffected during catalysis. Substrates **1a**, **1e**, **1k**, and **1l** were also subjected to transfer hydrogenation reactions using **Ir1′** (Table S3†). The results showed that **Ir1′** was just as efficient as **Ir1**, giving ≥90% yields of **2a**, **2e**, **2k**, and **2l**, respectively. Neither **Ir1** nor **Ir2** with HCOONa were able to reduce 4-formylpyridine **1y** (Fig. S34†), presumably due to pyridine coordination to Ir.[59] Surprisingly, we observed significant yield differences between **Ir1** *vs.* **Ir2** for products **2e** (97 *vs.* 19%), **2g** (99 *vs.* <5%), **2i** (99 *vs.* 17%), and **2k** (91 *vs.* <5%). Since the iridium centers in **Ir1**, **Ir1′**, and **Ir2** are electronically similar according to their IR spectral data, the differences are not likely due to electronic effects. We can rule out steric effects because the bulky 4-isopropylbenzaldehyde (**1b**) and 4-phenylbenzaldehyde (**1c**) substrates were readily reduced by **Ir2**/HCOONa. Based on our catalyst structure studies (*vide infra*), we hypothesize that substrates containing nucleophilic groups (*e.g.*, hydroxy, alkoxy, or amino) are capable of binding to the iridium center *via* their substituents and are slow to dissociate inside the supramolecular **Ir2** + Na^+ structure. In contrast, because **Ir1** and **Ir1′** are not spatially confined, re-orientation of the substrates to favor hydride transfer to the electrophilic C=O moiety is more facile.

We expanded our substrate scope studies to include other aldehydes (Fig. 2B). Using our typical reaction conditions, we screened aliphatic (**1m**), α,β-unsaturated (**1n**, **1o**), aromatic (**1p–1s**), and acetaldehyde substrates (**1t–1u**). Both **Ir1** and **Ir2** with HCOONa gave similar yields of **2m**, **2n** (both C=O and C=C bonds were reduced), and **2o**. For all other alcohol products, the monoiridium catalyst afforded significantly greater yields (>20%) than the diiridium catalyst, indicating that the former is more promiscuous toward substrates. The influence of spatial confinement in **Ir2** is most apparent when comparing the reaction yields between chemically similar substrates. For example, **Ir2** gave higher yields of **2q** (70%) than its structural isomer **2p** (51%) since the aldehyde group in **1q** is less sterically shielded than that in **1p**. Similarly, **Ir2** produced **2t** (55% yield) with much higher efficiency than **2u** (<5% yield). The two α-phenyl groups in **1u** likely make the substate too bulky to engage in hydride exchange with the Ir catalyst and formate. Overall, our results clearly showed that **Ir2** favors substrates with less sterically accessible aldehyde groups. The ability to differentiate molecular species based on shape and size has not been achieved using conventional half-sandwich catalysts (*e.g.*, **Ir1** or **Ir1′**).

In the context of bioorthogonal chemistry, catalysts that exhibit controlled reactivity are desirable because they can target specific substrates without negatively impacting other biological components.[1,2] As a representative example of an essential biomolecule, hydrocortisone (**1v**)[60] was tested as a potential substrate in transfer hydrogenation (Fig. 2B). When **Ir1** and HCOONa were combined with **1v** in D_2O/DMSO-d_6 at 37 °C, reduction of the C3 carbonyl group to **2v** was observed (Fig. S5†).[61] Up to 21% yield of **2v** was obtained after 24 h. In contrast, when **Ir2** was used as the catalyst, conversion of **1v** to **2v** did not occur after the same time period (Fig. S7†).

Since many essential aldehydes (*e.g.*, pyridoxal phosphate, retinal, glyceraldehyde-3-phosphate, *etc.*) are bulky whereas toxic aldehydes (*e.g.*, acrolein, malondialdehyde, *etc.*) are non-bulky,[62–64] **Ir2** could potentially be used as a selective detoxification agent.[55–57] For example, our data showed that reduction of the natural aldehyde vanillin **1i** by **Ir2**/HCOONa is relatively inefficient (17% yield, Fig. 2A). Because vanillin has more potent antioxidant effects than the corresponding vanillyl alcohol, it is desirable to avoid reducing **1i** inside the cell.[65–68] In contrast, we found that the cell-damaging aldehydes crotonaldehyde (**1o**, Fig. 2B), 4-hydroxynon-2-enal (Table S11,† entry 2), and hexa-2,4-dienal (Table S11,† entry 3) were converted to their corresponding non-toxic alcohol products by **Ir2**/HCOONa with high yields under our standard reaction conditions. Although further studies are needed to test the selectivity of **Ir2** inside live cells, our results suggest that it exhibits a key feature of bioorthogonal catalysts by virtue of its ability to differentiate between beneficial *vs.* harmful substances.[2]

Based on previous studies,[47,69] transfer hydrogenation reactions using Ir catalysts can proceed *via* several pathways (Fig. 3A). The productive route involves reaction of the Ir catalyst with HCOONa to generate an iridium–hydride (Ir–H) intermediate, which can react further with aldehydes to give alcohol products. Alternatively, the Ir–H species can reduce O_2 to generate H_2O_2.[69] When thiols are present, such as glutathione, cysteine (Cys), or homocysteine (Hsc), they can deactivate the Ir centers *via* coordination inhibition. The presence of H_2O_2 in the reaction mixture could lead to the conversion of thiols to disulfides, which are non-coordinating. Oxidation of aldehydes to carboxylic acids by H_2O_2 can also occur, but this process is slower than its reduction under our reaction conditions (Tables S5 and S9†).

To examine the thiol tolerance of the iridium complexes, we measured their ability to generate H_2O_2 in the presence and absence of glutathione (Fig. 3B). The iridium catalyst (50 μM of **Ir1** or 25 μM of **Ir2**) was combined with HCOONa (45 mM) and GSH (50 μM) in H_2O/DMSO (9 : 1) and stirred under air at 37 °C.

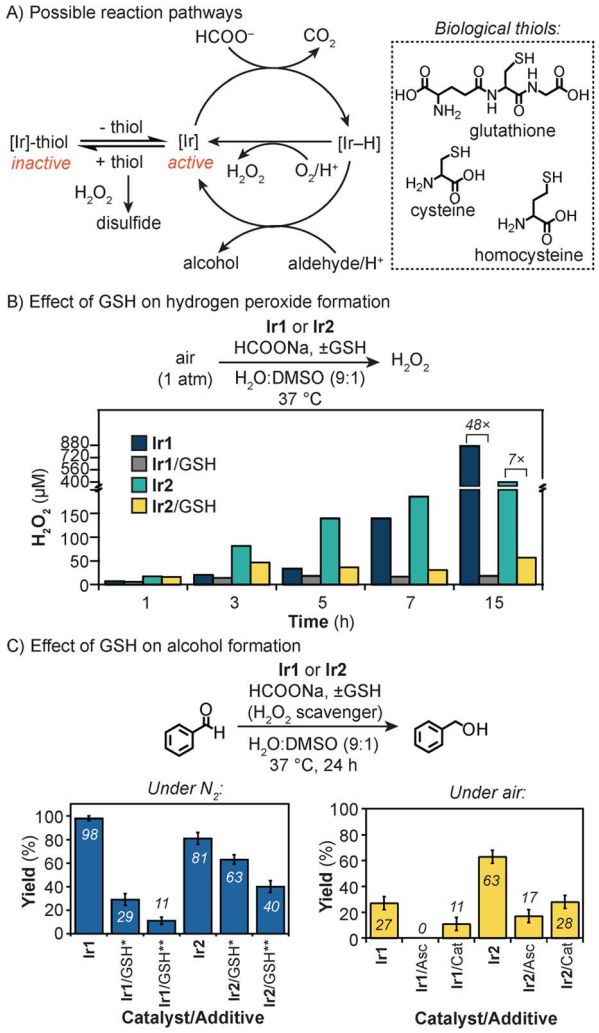

Fig. 3 Possible reactions of iridium catalysts during the transfer hydrogenation process (A) and the effects of GSH on H_2O_2 (B) and alcohol product formation (C). Amounts used: Ir complex (0.15 μmol of **Ir1**, 0.075 μmol of **Ir2**), HCOONa (135 μmol), GSH (up to 3.0 μmol), **1a** (15 μmol, if any), Asc (6 μmol, if any), Cat (1000 units per mL, if any) in H_2O/DMSO (9 : 1, 3 mL) at 37 °C, 24 h. Single asterisk (*) = 1.5 μmol; double asterisk (**) = 3.0 μmol. Abbreviations: Asc = sodium ascorbate, Cat = catalase.

The formation of hydrogen peroxide was monitored using commercial semi-quantitative H_2O_2 test strips (Fig. S14 and S15†).[69] Our results showed that in all reactions, H_2O_2 concentrations increased with and without GSH over the course of 15 h. However, the addition of GSH to **Ir1** led to a 48-fold inhibition in H_2O_2 formation (870 *vs.* 18 μM), whereas the addition of GSH to **Ir2** led to only a 7-fold inhibition (401 *vs.* 57 μM). These observations indicate that **Ir2** is less sensitive to thiols than **Ir1**. Since GSH is a relatively large small-molecule, it may not bind to **Ir2** as readily as **Ir1** due to its protected active sites.

Next, we investigated the effects of thiols on the reduction of benzaldehyde by the Ir catalysts and HCOONa. The first set of experiments was carried out under N_2 to suppress the formation of H_2O_2 (Fig. 3C and Table S4†). When GSH (1 mM) was added to **Ir1** (50 μM) and HCOONa (45 mM) in H_2O/DMSO (9 : 1), the conversion of **1a** to **2a** dropped by 8.9-fold, relative to the standard reaction without GSH (11 *vs.* 98% yield, respectively). In comparison, the addition of GSH (1 mM) to **Ir2** (25 μM) only lowered the activity by about 2.0-fold with respect to the control (40 *vs.* 81% yield, respectively).

A second set of experiments was conducted in air to mimic the aerobic environment of mammalian cells. We found that in the presence of 0.5 mM of GSH, reduction of **1a** by **Ir1** (50 μM) or **Ir2** (25 μM) and HCOONa (45 mM) gave 27 and 63% yield of **2a**, respectively (Fig. 3C). To minimize oxidation of GSH (Fig. S8†), the reactions were treated with either the anti-oxidant sodium ascorbate (Asc) or H_2O_2-disproportionating enzyme catalase (Cat) (Table S5†). As expected, the yields of benzyl alcohol decreased due to the availability of more GSH to deactivate the Ir catalysts. For example, the addition of Cat to **Ir1** or **Ir2** gave **2a** in 11 and 28% yield, respectively. Once again, however, reactions with **Ir2** generated more transfer hydrogenation products than those with **Ir1**, demonstrating that the sterically protected **Ir2** exhibit better thiol tolerance. The catalyst inhibiting effects of GSH could be reversed by introducing thiol scavengers such as Michael acceptors or chemical oxidants (Table S6†).[24,70]

Under similar reaction conditions, the use of Cys or Hcy instead of GSH completely deactivated the iridium catalysts (Fig. S12†). Since Cys and Hcy are single amino acids rather than a tripeptide like GSH, their smaller size may allow them to bind **Ir2** more readily. Finally, thioethers (*e.g.*, methionine) and disulfides (*e.g.*, cystine and GSH disulfide) have minimal effects on the Ir catalysts.

Because the macrocyclic backbone in **Ir2** features multiple amide donors, we wondered if they could chelate cations with different affinities.[71,72] This interaction could tune simultaneously the steric and electronic properties of the Ir centers, leading to corresponding changes in their substrate reactivity. We found that when **Ir2** and **1p** were treated with HCOOLi, HCOONa, HCOOK, or HCOOCs under our standard transfer hydrogenation conditions, **2p** (indicated as ** in Fig. 4) was produced in 17, 38, 34, and 41% yield, respectively. However,

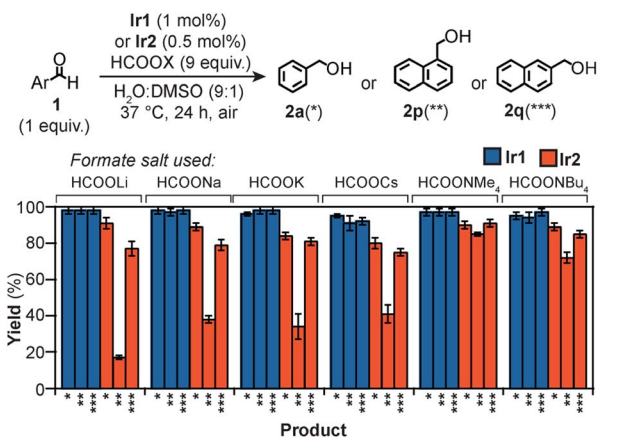

Fig. 4 Transfer hydrogenation reactions using Ir catalysts and various formate salts. Reaction conditions used: substrate (15 μmol), formate salt (135 μmol), Ir complex (0.15 μmol of **Ir1**, 0.075 μmol or **Ir2**), 37 °C, 24 h. See Table S7† for specific yields.

switching the formate salt to either $HCOONMe_4$ or $HCOONBu_4$ gave significantly larger quantities of **2p** (>70% yield). It appears that the behavior of **Ir2** is strongly dependent on the identity of the cation used. Because **1p** is sensitive to the Ir environment due to its sterically crowded C=O group, these results suggest that the catalyst structure is more confined in the reaction with alkali ions than with tetraalkylammonium ions. For some substrates, the amount of product generated was independent of X in HCOOX. For example, the reduction of **1a** and **1q** to the corresponding alcohol **2a** (*) and **2q** (***), respectively, proceeded with ≥75% yield for all formate salts tested. Because the aldehyde moiety in **1a** and **1q** is unhindered, these substrates can be readily reduced regardless of **Ir2**'s spatial arrangement.

For comparison, we performed similar reactions using the monoiridium catalysts. Our results showed that **Ir1** gave quantitative yields of **2a**, **2p**, and **2q** with all HCOOX salts (Fig. 4), suggesting that the identity of X had no impact on the catalyst activity.

Next, further studies were performed to interrogate the nature of the **Ir2**–Lewis acid interaction. First, we studied the binding of Na^+ to the iridium complexes in H_2O/DMSO (9 : 1) using UV-vis absorption spectroscopy (Fig. 5A). When NaCl was added to a solution containing **Ir1**, no spectral changes were observed, indicating that Na^+ does not bind to the Ir complex. In contrast, when **Ir2** was treated with NaCl, the mixture became cloudy and its UV-vis absorption baseline increased. This effect was also observed when NaCl was replaced with $NaPF_6$ (Fig. S20†). Titration of **Ir2** with NMe_4Cl, which contains a non-coordinating ammonium cation, resulted in no spectral changes (Fig. S24†). These observations indicate that **Ir2** binds preferentially to Lewis acidic cations, whereas **Ir1** does not.

Second, to obtain structural characterization of the **Ir2** complex in the presence of Lewis acids, X-ray crystallography was used. Single crystals were grown by layering pentane over a dichloromethane solution of **Ir2** containing trace amounts of NaCl. Crystallographic analysis showed the presence of a multinuclear species with the formula $[(\mathbf{Ir2})_2Na(H_2O)]Cl$ (**Ir2**–Na) (Fig. 5B). This complex features two **Ir2** units coordinated to a central Na^+ ion *via* the amide groups of their ligand backbone. The iridium centers adopt the expected half-sandwich structure and the sodium center is five-coordinate due to binding with an additional water molecule. A chloride counteranion was also located within the crystallographic asymmetric unit.

Third, to determine whether the structure of **Ir2**–Na is representative of the species in bulk solution, we used dynamic light scattering (DLS) to measure the **Ir2** + NaCl particles in various aqueous mixtures (Fig. 5C). DLS analysis of a H_2O/DMSO (9 : 1) solution containing 50 μM of **Ir2** and 2 mM of NaCl showed the presence of particles with a diameter of ~290 nm. Since biological media contains significant amounts of Lewis acids, we also prepared samples of **Ir2** in PBS/DMSO (9 : 1) (Fig. S23†). The commercial PBS used is composed of KCl (2.7 mM), NaCl (137 mM), Na_2HPO_4 (10 mM), and KH_2PO_4 (1.8 mM). Analysis of this heterogeneous solution by DLS showed that the particles formed have an average size of ~639 nm. Similarly, large nanoassemblies (>750 nm) were observed when **Ir2** was measured in the cell culture media Dulbecco's Modified Eagle Medium (DMEM) (Fig. S27 and S28†), which also contains high salt concentrations. Based on the molecular structure of **Ir2**–Na, the longest length of a single **Ir2** complex is ~1.8 nm. Thus, each **Ir2** + NaCl particle must contain hundreds of **Ir2** species. However, it is unclear whether the **Ir2** + Lewis acid particles comprise aggregates of discrete clusters or a continuous metal–organic network. Although our cell uptake data showed that **Ir2** is internalized inside cells, it is uncertain whether the complex is taken up as a discrete molecular species or nanoassembly.[52,73–75]

Our investigations led to several key findings. First, the macrocyclic effect is critical in enabling **Ir2** to form adducts with Lewis acids, since **Ir1** and **Ir1′** lack this ability despite also possessing backbone amides. Second, the **Ir2**–Lewis acid nanoassemblies are likely porous because some substrates were reduced with high efficiency (*e.g.*, **1a–1d**, **1h**, **1l**, **1m**, and **1n**). Presumably, the supramolecular motif allows small molecules to diffuse in and out of the active sites but at the same time, restricts access to species bearing nucleophilic substituents (*e.g.*, **1e**, **1g**, **1i**, **1j**, **1k**, and **1y**) or sterically hindered C=O groups (*e.g.*, **1r**, **1u**, and **1v**). Our results also suggest that the confined

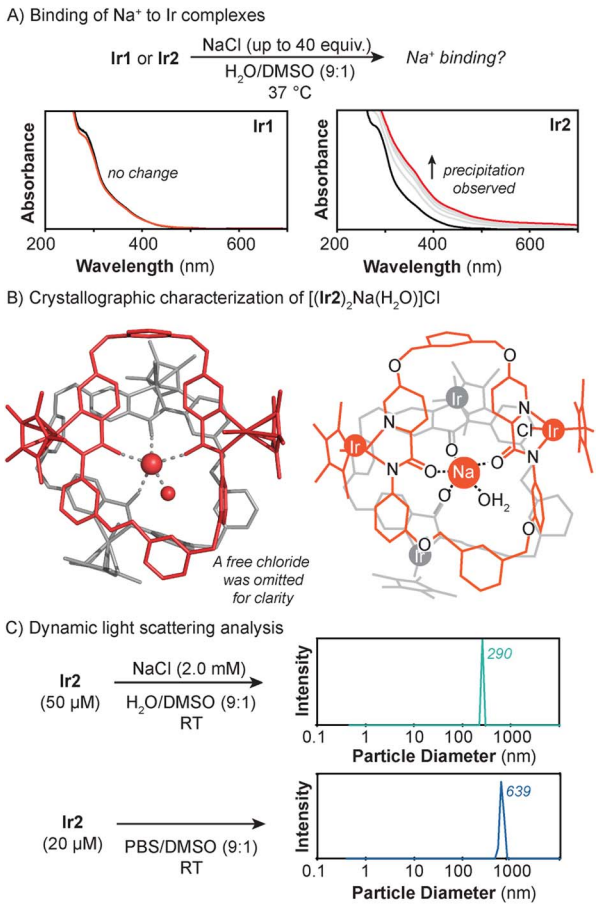

Fig. 5 Characterization of the **Ir2** + Lewis acid species using UV-vis absorption spectroscopy (A), single crystal X-ray crystallography (B), and dynamic light scattering (C). In part B, the X-ray structure (left) and cartoon representation (right) of $[(\mathbf{Ir2})_2Na(H_2O)]Cl$ are shown in gray and red-orange to highlight the presence of two different **Ir2** units.

active sites in the **Ir2**–Lewis acid nanoassemblies disfavor binding by GSH, which allows the free thiols to scavenge H_2O_2 and further increase the Ir catalyst's reaction efficiency. Third, substrate selectivity may be further tuned by judicious selection of the Lewis acid. For example, using Li^+ gave lower yields of **2p** than using Na^+, K^+, or Cs^+ (Fig. 4). A comparison of the IR spectra of **Ir2** with and without NaCl did not reveal any significant differences (Fig. S31†). However, further studies are needed to determine how the binding of different cations changes the structural and electronic properties of the **Ir2** supramolecular motif. Although Korendovych and coworkers have reported an elegant example using Cp*Ir nanoassemblies for enantioselective transfer hydrogenation reactions,[76] their vesicle-like structures were formed *via* hydrophobic interactions rather than metal–ligand coordination. Lastly, although the intrinsic activity of **Ir1** is higher than **Ir2** + Lewis acid because the former has a more sterically accessible active site (Fig. 3C, left), **Ir2** + Lewis acid showed higher activity when reactions were conducted in the presence of GSH and air (Fig. 3C, right). Thus, when developing catalysts for bioorthogonal chemistry applications, it is important to consider how they might perform under cell-like rather than controlled synthetic environments.

Conclusions

In summary, we present a new strategy to design bioorthogonal catalysts by leveraging Lewis acid-driven coordination self-assembly. Our macrocyclic construct **Ir2** was demonstrated to be a highly active catalyst for transfer hydrogenation reactions under physiologically relevant conditions. In the presence of Lewis acids, **Ir2** tolerates up to 1.0 mM of GSH and reacts preferentially with small aldehydes. Their ability to discriminate substrates based on shape and size could have useful biological applications, such as the selective detoxification of toxic aldehydes over essential aldehydes. Our studies suggest that the unique reactivity of the **Ir2**–Lewis acid nanoassemblies stems from the spatial confinement of the Ir centers in a supramolecular framework. Although the exact nature of this extended structure is currently under investigation, the preorganized amide donors in **Ir2** are likely responsible for its ability to form stable adducts with secondary cations. Our MIC confinement approach is advantageous over other methods because it can be applied *in situ* by exploiting naturally occurring salts in biological media (*e.g.*, Li^+, Na^+, K^+, *etc.*). Based on preliminary cell studies, **Ir2** is non-toxic when used at low concentrations (*i.e.*, below its IC_{50} value of 85 μM in NIH-3T3 cells). However, the extent to which its reactivity in the flask is replicated inside living cells and its cellular uptake mechanism need to be investigated. Finally, we are also exploring advanced applications, such as exploiting the heterogeneous cellular environment to achieve dynamic or switchable self-assembly.[49] Importantly, this work expands the options available for developing metal-based intracellular catalysts, which will likely provide new opportunities for bioorthogonal chemistry discovery.

Data availability

Crystallographic data for **Ir2**-Na has been deposited at the CCDC under 2267222. The data supporting this article have been uploaded as part of the ESI.†

Author contributions

H. D. N.: conceptualization, investigation, analysis, writing. R. D. J.: investigation, editing. D. T. C.: investigation. T. V. T.: conceptualization, editing. L. H. D.: conceptualization, analysis, writing, supervision.

Conflicts of interest

There are no conflicts to declare.

Acknowledgements

We are grateful to the Welch Foundation (Grant No. E-1894 to L. H. D.) and the National Institutes of Health (Grant No. R01GM129276 to L. H. D.) for funding this work. We thank Mina Omidiyan, Jong Moon Lee, and Prof. T. Randall Lee for assisting and allowing us to access their dynamic light scattering instrument.

References

1 E. M. Sletten and C. R. Bertozzi, *Angew. Chem., Int. Ed.*, 2009, **48**, 6974–6998.
2 S. L. Scinto, D. A. Bilodeau, R. Hincapie, W. Lee, S. S. Nguyen, M. Xu, C. W. am Ende, M. G. Finn, K. Lang, Q. Lin, J. P. Pezacki, J. A. Prescher, M. S. Robillard and J. M. Fox, *Nat. Rev. Methods Primers*, 2021, **1**, 30.
3 M. M. A. Mitry, F. Greco and H. M. I. Osborn, *Chem.–Eur. J.*, 2023, **29**, e202203942.
4 E. Kim and H. Koo, *Chem. Sci.*, 2019, **10**, 7835–7851.
5 J. Dommerholt, F. P. J. T. Rutjes and F. L. van Delft, *Top. Curr. Chem.*, 2016, **374**, 16.
6 B. L. Oliveira, Z. Guo and G. J. L. Bernardes, *Chem. Soc. Rev.*, 2017, **46**, 4895–4950.
7 H. Madec, F. Figueiredo, K. Cariou, S. Roland, M. Sollogoub and G. Gasser, *Chem. Sci.*, 2023, **14**, 409–442.
8 A. Seoane and J. L. Mascareñas, *Eur. J. Org Chem.*, 2022, e202200118.
9 J. J. Soldevila-Barreda and N. Metzler-Nolte, *Chem. Rev.*, 2019, **119**, 829–869.
10 A. H. Ngo, S. Bose and L. H. Do, *Chem.–Eur. J.*, 2018, **24**, 10584–10594.
11 S. Gutiérrez, M. Tomás-Gamasa and J. L. Mascareñas, *Chem. Sci.*, 2022, **13**, 6478–6495.
12 N. Li, R. K. V. Lim, S. Edwardraja and Q. Lin, *J. Am. Chem. Soc.*, 2011, **133**, 15316–15319.
13 S. N. W. Toussaint, R. T. Calkins, S. Lee and B. W. Michel, *J. Am. Chem. Soc.*, 2018, **140**, 13151–13155.
14 N. S. Schunck and S. Mecking, *Angew. Chem., Int. Ed.*, 2022, **61**, e202211285.

15 C. Streu and E. Meggers, *Angew. Chem., Int. Ed.*, 2006, **45**, 5645–5648.
16 M. I. Sánchez, C. Penas, M. E. Vázquez and J. L. Mascareñas, *Chem. Sci.*, 2014, **5**, 1901–1907.
17 M. Tomás-Gamasa, M. Martínez-Calvo, J. R. Couceiro and J. L. Mascareñas, *Nat. Commun.*, 2016, **7**, 12538.
18 N. Singh, A. Gupta, P. Prasad, P. Mahawar, S. Gupta and P. K. Sasmal, *Inorg. Chem.*, 2021, **60**, 12644–12650.
19 S. Bose, A. H. Ngo and L. H. Do, *J. Am. Chem. Soc.*, 2017, **139**, 8792–8795.
20 J. P. C. Coverdale, I. Romero-Canelón, C. Sanchez-Cano, G. J. Clarkson, A. Habtemariam, M. Wills and P. J. Sadler, *Nat. Chem.*, 2018, **10**, 347–354.
21 S. Gutiérrez, M. Tomás-Gamasa and J. L. Mascareñas, *Angew. Chem., Int. Ed.*, 2021, **60**, 22017–22025.
22 A. Gutierrez-Gonzalez, D. Marcos-Atanes, L. G. Cool, F. Lopez and J. L. Mascareñas, *Chem. Sci.*, 2023, **14**, 6408–6413.
23 C. Vidal, M. Tomás-Gamasa, A. Gutiérrez-González and J. L. Mascareñas, *J. Am. Chem. Soc.*, 2019, **141**, 5125–5129.
24 Y. M. Wilson, M. Dürrenberger, E. S. Nogueira and T. R. Ward, *J. Am. Chem. Soc.*, 2014, **136**, 8928–8932.
25 H. D. Nguyen and L. H. Do, *Curr. Opin. Chem. Biol.*, 2022, **71**, 102213.
26 A. Sathyan, L. Deng, T. Loman and A. R. A. Palmans, *Catal. Today*, 2023, **418**, 114116.
27 D. Diao, A. J. Simaan, A. Martinez and C. Colomban, *Chem. Commun.*, 2023, **59**, 4288–4299.
28 Y. Liu, K. L. Lai and K. Vong, *Eur. J. Inorg. Chem.*, 2022, e202200215.
29 B. Maity, M. Taher, S. Mazumdar and T. Ueno, *Coord. Chem. Rev.*, 2022, **469**, 214593.
30 S. Liu, P. Du, H. Sun, H.-Y. Yu and Z.-G. Wang, *ACS Catal.*, 2020, **10**, 14937–14958.
31 Y. Okamoto and T. R. Ward, *Angew. Chem., Int. Ed.*, 2017, **56**, 10156–10160.
32 M. Basauri-Molina, C. F. Riemersma, M. A. Würdemann, H. Kleijn and R. J. M. Klein Gebbink, *Chem. Commun.*, 2015, **51**, 6792–6795.
33 M. Taher, B. Maity, T. Nakane, S. Abe, T. Ueno and S. Mazumdar, *Angew. Chem., Int. Ed.*, 2022, **61**, e202116623.
34 S. C. Bete and M. Otte, *Angew. Chem., Int. Ed.*, 2021, **60**, 18582–18586.
35 G. Izzet, J. Zeitouny, H. Akdas-Killig, Y. Frapart, S. Ménage, B. Douziech, I. Jabin, Y. Le Mest and O. Reinaud, *J. Am. Chem. Soc.*, 2008, **130**, 9514–9523.
36 D. Zhang, K. Jamieson, L. Guy, G. Gao, J.-P. Dutasta and A. Martinez, *Chem. Sci.*, 2017, **8**, 789–794.
37 J. G. Rebelein, Y. Cotelle, B. Garabedian and T. R. Ward, *ACS Catal.*, 2019, **9**, 4173–4178.
38 Y. Bai, X. Feng, H. Xing, Y. Xu, B. K. Kim, N. Baig, T. Zhou, A. A. Gewirth, Y. Lu, E. Oldfield and S. C. Zimmerman, *J. Am. Chem. Soc.*, 2016, **138**, 11077–11080.
39 J. Chen, E. S. Garcia and S. C. Zimmerman, *Acc. Chem. Res.*, 2020, **53**, 1244–1256.
40 G. Qiu, P. Nava, A. Martinez and C. Colomban, *Chem. Commun.*, 2021, **57**, 2281–2284.
41 C.-M. Hirschbiegel, X. Zhang, R. Huang, Y. A. Cicek, S. Fedeli and V. M. Rotello, *Adv. Drug Delivery Rev.*, 2023, **195**, 114730.
42 Y. Fan, S. Liu, Y. Yi, H. Rong and J. Zhang, *ACS Nano*, 2021, **15**, 2005–2037.
43 R. M. Yusop, A. Unciti-Broceta, E. M. V. Johansson, R. M. Sánchez-Martín and M. Bradley, *Nat. Chem.*, 2011, **3**, 239–243.
44 M. A. Miller, B. Askevold, H. Mikula, R. H. Kohler, D. Pirovich and R. Weissleder, *Nat. Commun.*, 2017, **8**, 15906.
45 L. A. Khawli and S. Prabhu, *Mol. Pharmaceutics*, 2013, **10**, 1471–1472.
46 A. H. Ngo, M. Ibañez and L. H. Do, *ACS Catal.*, 2016, **6**, 2637–2641.
47 A. H. Ngo and L. H. Do, *Inorg. Chem. Front.*, 2020, **7**, 583–591.
48 W. A. Catterall, M. J. Lenaeus and T. M. Gamal El-Din, *Annu. Rev. Pharmacol. Toxicol.*, 2020, **60**, 133–154.
49 T. Dudev and C. Lim, *Chem. Rev.*, 2014, **114**, 538–556.
50 G. Moreno-Alcántar and A. Casini, *FEBS Lett.*, 2023, **597**, 191–202.
51 S. V. Dummert, H. Saini, M. Z. Hussain, K. Yadava, K. Jayaramulu, A. Casini and R. A. Fischer, *Chem. Soc. Rev.*, 2022, **51**, 5175–5213.
52 G. Moreno-Alcántar, *Eur. J. Inorg. Chem.*, 2023, **26**, e202200788.
53 S. Lo, C. Z.-J. Ren, P. Solís-Muñana and J. L.-Y. Chen, in *Supramolecular Nanotechnology*, 2023, pp. 469–493.
54 C. C. James, B. de Bruin and J. N. H. Reek, *Angew. Chem., Int. Ed.*, 2023, e202306645.
55 Z. Xie, S. P. Baba, B. R. Sweeney and O. A. Barski, *Chem.-Biol. Interact.*, 2013, **202**, 288–297.
56 L. T. Beringer, S. Li, G. Gilmore, J. Lister and S. Averick, *Mol. Pharmaceutics*, 2015, **12**, 3776–3781.
57 R. D. Jana, A. H. Ngo, S. Bose and L. H. Do, *Chem.–Eur. J.*, 2023, e202300842.
58 Z. Almodares, S. J. Lucas, B. D. Crossley, A. M. Basri, C. M. Pask, A. J. Hebden, R. M. Phillips and P. C. McGowan, *Inorg. Chem.*, 2014, **53**, 727–736.
59 A. C. Carrasco, V. Rodríguez-Fanjul and A. M. Pizarro, *Inorg. Chem.*, 2020, **59**, 16454–16466.
60 L. M. Mongioì, R. A. Condorelli, F. Barbagallo, S. La Vignera and A. E. Calogero, *Endocrine*, 2020, **67**, 507–515.
61 A. H. Ngo, M. J. Adams and L. H. Do, *Organometallics*, 2014, **33**, 6742–6745.
62 R. M. LoPachin and T. Gavin, *Chem. Res. Toxicol.*, 2014, **27**, 1081–1091.
63 S. Dalleau, M. Baradat, F. Guéraud and L. Huc, *Cell Death Differ.*, 2013, **20**, 1615–1630.
64 D. T. Nam, M. Arseneault, V. Murthy and C. Ramassamy, *Curr. Mol. Pharmacol.*, 2010, **3**, 66–78.
65 D. P. Bezerra, A. K. N. Soares and D. P. de Sousa, *Oxid. Med. Cell. Longevity*, 2016, **2016**, 9734816.
66 D. Zhao, J. Sun, B. Sun, M. Zhao, F. Zheng, M. Huang, X. Sun and H. Li, *RSC Adv.*, 2017, **7**, 46395–46405.
67 A. Tai, T. Sawano, F. Yazama and H. Ito, *Biochim. Biophys. Acta, Gen. Subj.*, 2011, **1810**, 170–177.
68 A. Tai, T. Sawano and F. Yazama, *Biosci., Biotechnol., Biochem.*, 2011, **75**, 2346–2350.

69 H. T. H. Nguyen and L. H. Do, *Chem. Commun.*, 2020, **56**, 13381–13384.
70 S. Li, L. Wang, F. Yu, Z. Zhu, D. Shobaki, H. Chen, M. Wang, J. Wang, G. Qin, U. J. Erasquin, L. Ren, Y. Wang and C. Cai, *Chem. Sci.*, 2017, **8**, 2107–2114.
71 J. W. Steed, *Coord. Chem. Rev.*, 2001, **215**, 171–221.
72 A. J. M. Miller, *Dalton Trans.*, 2017, **46**, 11987–12000.
73 M. Mauro, A. Aliprandi, D. Septiadi, N. S. Kehr and L. De Cola, *Chem. Soc. Rev.*, 2014, **43**, 4144–4166.
74 A. Aliprandi, M. Mauro and L. De Cola, *Nat. Chem.*, 2016, **8**, 10–15.
75 K. Kettler, K. Veltman, D. van de Meent, A. van Wezel and A. J. Hendriks, *Environ. Toxicol. Chem.*, 2014, **33**, 481–492.
76 M. A. Dolan, P. N. Basa, O. Zozulia, Z. Lengyel, R. Lebl, E. M. Kohn, S. Bhattacharya and I. V. Korendovych, *ACS Nano*, 2019, **13**, 9292–9297.